



Università di Pisa

Facoltà di Scienze Matematiche, Fisiche e Naturali

Corso di Laurea in Fisica

Anno Accademico 2009/2010

Tesi di Laurea

**Characterization of the Photon Calibrator
data from LIGO's sixth Science Run**

Candidato:
Alberto Sottile

Relatore:
Prof. Francesco Fidecaro

“Life is like riding a bicycle. To keep your balance you must keep moving.”
Albert Einstein

Contents

Introduction	iii
1 The search for gravitational waves	1
1.1 Gravitational waves and LIGO	1
1.2 The calibration of the interferometers	3
2 The Photon Calibrator	6
2.1 Principle of operation	6
2.2 Experimental setup	7
2.3 Computing the voice coil actuation coefficient	9
2.4 The Photon Calibrator Code	11
3 Characterization of the data	13
3.1 Removing outliers	13
3.2 Identification of a linear trend in the data	16
3.3 Statistical description of the data	18
3.4 Averaging the data	19
3.5 Long-term trend plots with averaged data	22
Conclusions	25
Bibliography	27

Introduction

The direct observation of gravitational waves, even though they were predicted one hundred years ago by the General Theory of Relativity, is one of the most pursued phenomena in contemporary physics. Accelerating, non-axisymmetric mass distributions radiate energy in the form of gravitational waves as they distort the fabric of space-time. However, even with current state-of-the-art sensors, ideal sources such as black holes and binary systems are not expected to generate signals detectable from Earth with event rates greater than one per several years. One of the ongoing efforts to detect this form of radiation, the Laser Interferometer Gravitational Wave Observatory (LIGO) project, has built two observatories. One is near Hanford, WA, and the other is near Livingston, LA. Both house 4-km-long Michelson interferometers which are ideally suited for detection of the quadrupolar strain in space-time induced by a gravitational wave.

Accurate and precise calibration of kilometer-scale interferometric gravitational wave detectors is crucial. Calibration errors in the instrument degrade its ability to detect and then to interpret the properties of any received signals. Several methods have been employed to calibrate the response of these interferometers to differential length variations. Most methods use interferometer configurations that are different than that used during searches for gravitational waves and induced displacements that are many orders of magnitude larger than those expected from gravitational waves. Moreover, the calibration function may change during the time when the interferometer is configured to detect gravitational waves. For these reasons it is necessary to develop a calibration procedure that can be used during the *Science Mode* operation of the detector, thus providing important information about the stability of the calibration without destabilizing the instrument. One such technique is the so-called Photon Calibrator.

The Photon Calibrator method uses an auxiliary, power-modulated laser reflected from the mirror at the end of one of the interferometer arms to induce calibrated displacements via the recoil of photons from the surface of the optic. Photon Calibrators have been operating continuously at both of LIGO's observatories during the entire Science Run, designated S6, that began on July 7, 2009 and is expected to end on October 6, 2010. The principal objective of

the Photon Calibrators during S6 was investigation of the long-term stability of the calibration of the actuators that control the lengths of the interferometer arms. Characterization of the Photon Calibrators data is the subject of the research for this thesis that was carried out while the author was resident at the LIGO Hanford Observatory for ten weeks during the summer of 2010.

Chapter 1

The search for gravitational waves

1.1 Gravitational waves and LIGO

One of the most important predictions of the General Theory of Relativity is the existence of gravitational waves. This theory depicts space and time as intimately connected, as a common fabric, known as space-time, that permeates the entire Universe. The Gravitational Force is not a force separate from the space-time. The gravitational field of a massive body is the way in which it curves space-time due to the presence of that body. This phenomenon causes another effect: every accelerating massive body radiates energy by distorting the fabric of space-time, the emission of gravitational waves. Just as electromagnetic waves are time-dependent vacuum solutions to Maxwell Equations, gravitational waves are time-dependent vacuum solutions to the Einstein Field Equations. Like electromagnetic waves, gravitational waves travel at the speed of light, transmitting the variations of the gravitational field in the space-time.

Despite this great generality, the weakness of gravity imposes stringent criteria on the bodies that can emit measurable amounts of energy via gravitational waves: only very massive astrophysical objects are candidates for being detectable sources of this form of radiation. Even strong sources of gravitational waves (black holes and Neutron Stars) that may exist in our galaxy or nearby galaxies are expected to radiate waves on Earth that do not exceed strains of one part in 10^{21} .

The intrinsic differential nature of the effects of a gravitational wave on a set of test masses makes the Michelson interferometers very efficient detection instruments, as they are extremely sensitive to changes in the relative lengths of the two orthogonal arms [1]. The Laser Interferometer Gravitational Wave Observatory (LIGO), as well as Virgo, use Michelson interferometers with Fabry-Perot arm cavities. An observatory in Hanford, WA houses two interfer-

ometers, a 4 km-long (“H1”) and a 2 km-long (“H2”, no longer active) detector, and an observatory in Livingston, LA houses a 4 km-long (“L1”) detector.

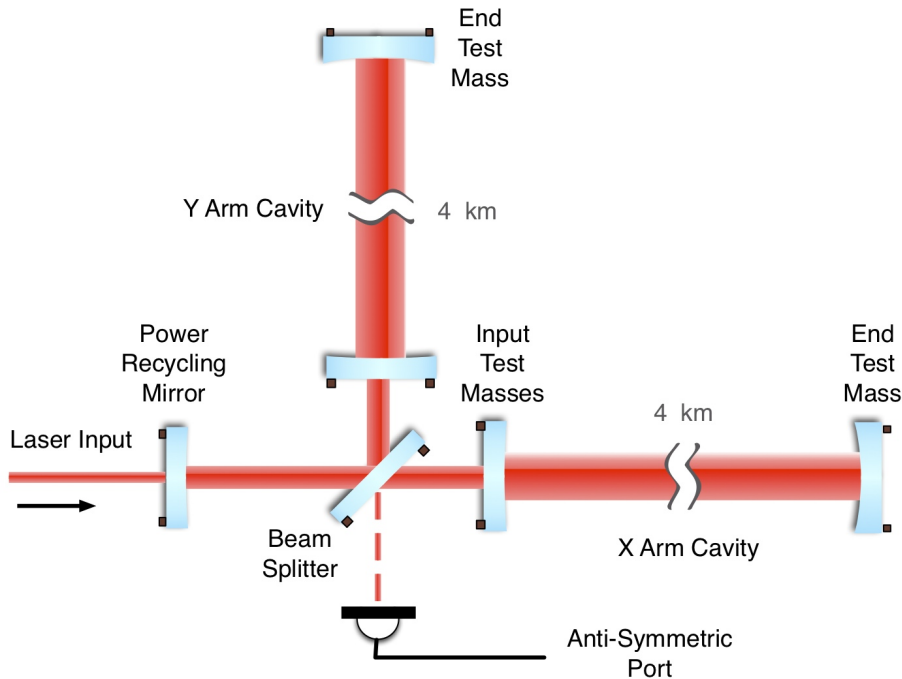


Figure 1.1: Schematic of the interferometers layout. Both the power-recycling mirror and the Fabry-Perot cavities are shown.

In all the interferometers of LIGO, the Fabry-Perot cavities enhance the sensitivity by resonating the laser light in the arms. The laser source emits a 20 W beam with a wavelength of 1064 nm. Power, mode and frequency are actively stabilized before the beam enters the interferometer. After that, the beam passes into the vacuum system: all of the main interferometer optical components and beam paths are enclosed in an ultra high vacuum. Each mirror in the beam path is suspended as a pendulum by a loop of steel wire, which provides vibration isolation. The pendulum suspension also allows free movement, in the transverse plane, of the test mass in the gravitational wave frequency band, from 40 Hz to 6 kHz. The position and orientation of a suspended optic is controlled by electromagnetic actuators: small magnets are bonded to the optic and coils are mounted to the support structure. Each arm contains a resonant Fabry-Perot optical cavity made up of a partially-reflective input mirror and a highly-reflective end mirror. The cavities cause the light to effectively reflect back and forth 100 times in each arm, thus increasing the strain and the phase shift caused by a gravitational wave. The cavities require an active feedback system. The round trip length of each cavity must be held to an integer multiple of the laser wavelength so that newly introduced light interferes constructively with light from previous round trips, so the light inside

the cavities resonates and increases in power [2].

The Michelson arm lengths are set such that the light interferes almost completely destructively at the antisymmetric port. This configuration is called dark fringe condition. A passing gravitational wave with polarization oriented along the arms, will impress a phase modulation on the light in each arm of the Michelson, with a relative phase shift of 180 degrees between the arms, when impinging normally to the interferometer. Only differential motion of the arms appears at the dark port, with an amplitude proportional to the wave strain and the input power. All of the instruments described above are supplemented with a set of sensors to monitor the local environment. Seismometers and accelerometers measure vibration, microphones monitor acoustic noise, magnetometers monitor fields. These sensors are used to detect external noises that could hinder gravitational wave detection.

The LIGO Scientific Collaboration decides when the interferometers are in commissioning or detection period. A detection period is called Science Run. Currently LIGO is in the sixth Science Run (S6), beginning on July 7, 2009 and ending on October 20, 2010. During a Science Run, the interferometers should be functional for 24 hours a day, every day. Of course, it is impossible to guarantee that the detector remains continuously in lock for the whole time, capable to detect successfully a gravitational wave. For example, external noises, e.g. an earthquake, wind or close human activities, could disturb or inhibit the functioning of the detector. The status of a detector when it is operating optimally is called Science Mode, because those data are fit for scientific analysis.

1.2 The calibration of the interferometers

Precise calibration of kilometer-scale interferometric gravitational wave detectors is crucial. Calibration errors in the instrument degrade its ability to detect and then to interpret the properties of any received signals. Passing gravitational waves that cause space to stretch and compress along the arm cavities would be sensed by the interferometer as differential changes in the lengths of the arms. Feedback control loops are used to maintain the nominal separation of the mirrors required for a signal detection. In particular, the differential arm length (DARM) control loop, depicted in figure (1.2), uses magnets glued to the back surfaces of the end test masses surrounded by coils of wire (called voice coil actuators) to control the positions of the suspended optics without touching the mirrors. The DARM readout signal is measured, amplified, filtered and then sent again to the voice coil actuators, to maintain the resonance condition in the interferometer.

When an external disturbance causes variations in the lengths of the arms,

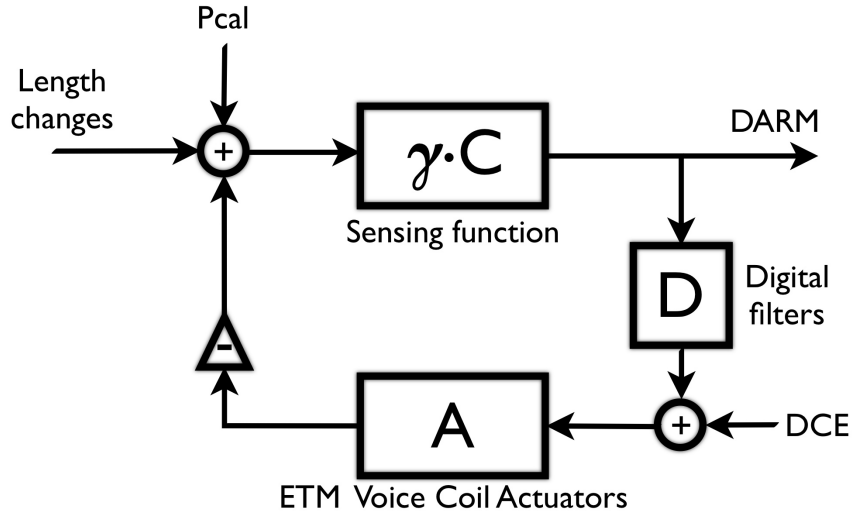


Figure 1.2: The Differential ARM control loop.

these change are sensed by the interferometer via the antisymmetric port ($\gamma \cdot C$ in figure (1.2)). This step is called sensing function, and its purpose is to convert length variations into a digital, calibrated signal. The readout of the sensing function is sent back to the loop. Digital filters (D) tailor the signal, which is then sent to the voice coil actuators. The actuators (A) drive the mirrors, via the coils, using the digital signal from the loop as a guide, to counter ($-$) the original length variation and maintain the DARM length near its original value. If all the parts of the loop are working correctly, length variations in the interferometer should be compensated by the reaction of the actuators. Calibrate the interferometer means to measure the DARM closed loop transfer function in response to a length fiducial. The DARM response function $R(f)$ allows conversion of the DARM signal to absolute displacement at all relevant frequencies. Multiplying the DARM readout signal by this response function yields the calibrated DARM error signal [3].

There are two ways to inject length variations in the loop. One is the recoil of the photons from the auxiliary power modulated laser on the mirror (Pcal). The other one uses the actuators as source of displacements. This excitation is called DARM Control Excitation (DCE) and is injected directly on the actuators. During S6 both the excitations were contemporary activated every time the interferometer was in Science Mode.

The complex interaction of this control loop with the mechanical plant, and with the possible gravitational waves makes the calibration of the instrument challenging.

Presently, the principal calibration method used for the LIGO interferometers is the Free-swinging Michelson technique. It relies on measurement of

Michelson interference fringes when the suspended optics are swinging freely. With the feedback control switched off, the free motion of the mirrors is measured both in the antisymmetric port and in the actuator coils: comparing those two measurements provides a length calibration of the antisymmetric photodetector and, thus, of the DARM signal. This calibration technique, due to its structure, can be used only to calibrate the whole DARM control loop, and not to measure the open loop transfer function [4].

The current generation of gravitational wave detectors are sensitive to DARM variations with amplitude spectral densities on the order of 10^{-19} m/ $\sqrt{\text{Hz}}$, at a frequency near 100 Hz [2].

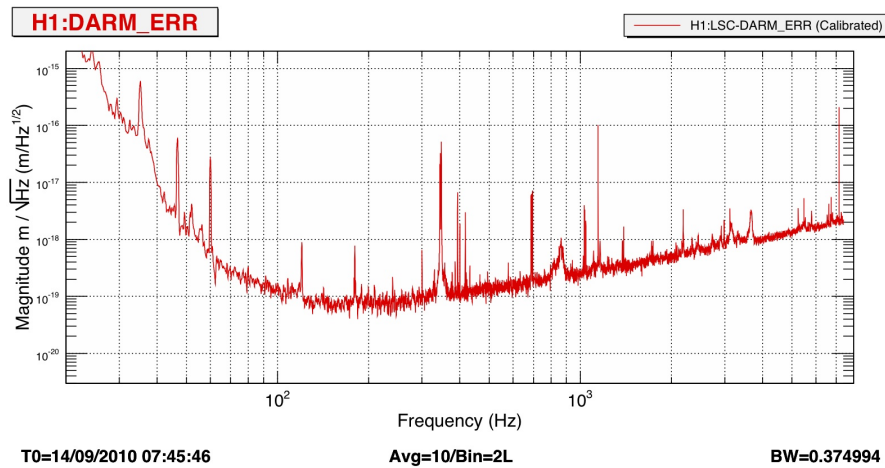


Figure 1.3: The DARM_ERR channel (Differential ARM ERRor) is a representation of the sensitivity of the interferometer at all the frequencies.

The working conditions of the interferometers change with time, and continuous or at least periodic calibrations are necessary. There are several methods to calibrate the test mass displacement and they are all employed to eliminate systematic errors in the calibration procedure. Unfortunately, in most cases the interferometer cannot detect gravitational waves during the calibration, because calibration methods need invasive operations or produce effects on the test mass displacements that are much larger than the expected apparent displacements that would be caused by the gravitational waves. At this time, the calibration of all the interferometers of the LIGO is done with an off-line method, which has several restrictions: because of the inability to acquire data during the calibration, one is forced to allow for long periods of time between two calibration runs and therefore the reliability required of the results is decreased. For these reasons it is necessary to develop a calibration procedure that can be used during the whole Science Run, thus providing important information about the stability of the calibration, without destabilizing the instrument. One of these techniques is the one so-called Photon Calibrator.

Chapter 2

The Photon Calibrator

2.1 Principle of operation

The Photon Calibrator method uses an auxiliary, power-modulated laser reflected on the end test masses (ETMs) to induce calibrated displacements via the recoil of photons from the surface of the mirror. The principle on which the Photon Calibrator relies is the comparison of the movement of the mirror induced by the photons against the movements of the same mirror induced by the voice coil actuators. The same optic is subjected to both the excitations, at different frequencies, at the same time. A measurement of the effects on the sensitivity of the interferometer caused by these perturbations allows the determination of the actuation coefficient of the corresponding actuator, which is the purpose of a calibration procedure. The laser source of the Photon Calibrator is located on an optical table outside of the vacuum system of the interferometer. It has a wavelength of 1047 nm, slightly different from that of the main beam, and an average power of 100 mW. Using an optical modulator the power is changed introducing a sinusoidal pattern with an amplitude of about 50 mW. Therefore, the exit power of the laser can be written as

$$P(t) = P_0 + P_m \sin(\omega t) \quad (2.1)$$

where P_0 is the average power, P_m is the amplitude of the power modulation and ω is its frequency. When the beam is incident upon the surface of the mirror, the beam reflects from the surface, transfers momentum from the recoiling photons and thus exerts a force on the mirror. Like in the case of the gravitational waves, if the frequency of the modulation is far above the pendulum resonance frequency of the suspension system, the mirror is essentially free to move in the horizontal plane. Thus, we can use the free-mass transfer function to determine the displacement of the optic.

$$F(t) = M\ddot{x}(t) = \frac{dp}{dt} \quad (2.2)$$

where M is the mass of the mirror. The impulse produced by the recoil of the photons from the test mass produces a change in the momentum of the optic. Every photon, reflecting from the mirror with an angle of incidence equal to θ , transfers a longitudinal momentum equal to $2 \hbar k \cos \theta$, where $k = 2\pi/\lambda = 2\pi\nu/c$ is the wavenumber of the laser source, λ is its wavelength, ν is its frequency, c is the speed of light, \hbar is the reduced Planck constant and the factor 2 is given by the elastic reflection of the photon. Thus, for a flux of n photons per second, the variation of momentum is

$$\frac{dp}{dt} = 2 n \hbar k \cos \theta = 2 n \hbar \cdot \frac{2 \pi \nu \cos \theta}{c} = \frac{2 n h \nu \cos \theta}{c} \quad (2.3)$$

If the laser source has a power of P , because every photon carries an energy of $h\nu$, the power of a source with n photons per second is

$$P = n h \nu \quad (2.4)$$

thus, due to the eq. (2.3) and the eq. (2.1),

$$\frac{dp}{dt} = \frac{2 n h \nu \cos \theta}{c} = \frac{2 P \cos \theta}{c} = \frac{P_m \sin(\omega t) \cos \theta}{c} \quad (2.5)$$

Because we are looking only for temporal variations of the momentum of the mass at the power modulation frequency, ω , we can disregard the constant component of the power. Using the equation (2.5) into the equation (2.2) gives

$$M \ddot{x}(t) = \frac{P_m \sin(\omega t) \cos \theta}{c} \quad (2.6)$$

Assuming that the solution of the equation (2.6) has the form of $x(t) = \sin(\omega t)$ for a power modulation that has this form, leads to the amplitude of the induced motion x_m , given by

$$x_m(\omega) = -\frac{2P_m \cos \theta}{Mc\omega^2} \quad (2.7)$$

The minus sign indicates that the motion is 180 degrees out of phase with the applied force [5].

2.2 Experimental setup

When the applied force is not directed through the center of mass of the optic, the induced torque caused an angular deflection of the test mass, that can degrade the calibration. However, the center of the mirrors is already used during the Science Mode by the main laser of the interferometer and it is undesirable to apply forces directly onto it, because of elastic deformation caused by the Photon Calibrator beam. Therefore, to avoid an angular displacement and, at the same time, allow the interferometer to be operational during calibration,

the Photon Calibrator uses two beams, instead of one, balanced in power and displaced symmetrically about the center of the face of the optic.

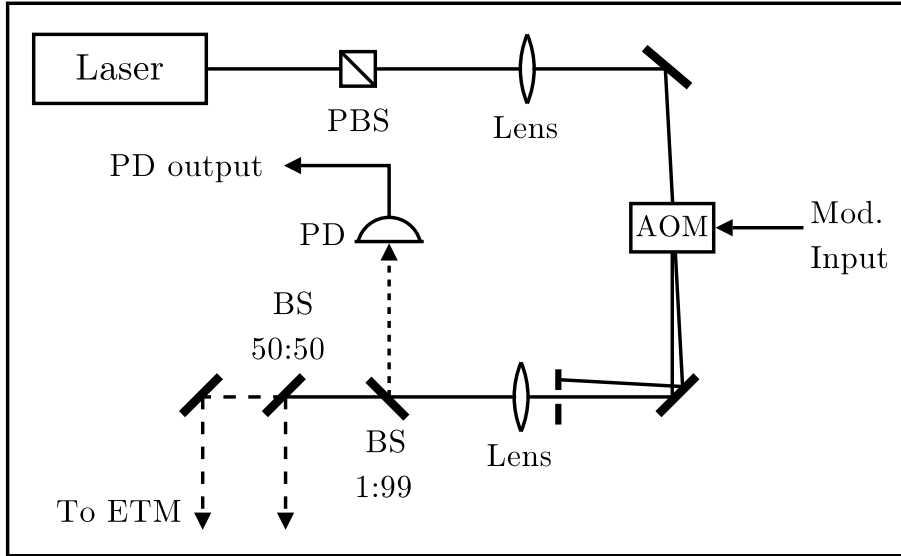


Figure 2.1: Optical table layout of the Photon Calibrator. The laser is sent to an acousto-optic modulator, which varies the power of the laser sinusoidally. This modulated laser is sent to a 99:1 beam splitter, the weaker fraction is used to measure the power modulation using a photodetector. The remaining 99% of the power crosses another 50:50 beam splitter, which creates the two parallel beams, with the same power, that will be sent to the end test mass [5].

After the power modulation, the laser is split in two portions via a beam splitter, which produces a secondary beam with 1% of the power. This fraction is sent to a photodetector that monitors the power directed to the test mass with high precision. The rest of the beam is sent to a second beam splitter, which divides the power in two equal parts, to prepare the two output beams. A calibration standard provides high accuracy calibration of the internal power monitor [6]. This optical layout is shown in figure (2.1).

The Photon Calibrator beams enter the vacuum envelope through a glass viewport and impinge on the test mass as shown in figure (2.2). The angle of incidence of both the beams is approximately 9.6 degrees. The laser power reflected from the test mass can be continuously monitored by computing the product of the photodetector signal with the overall optical efficiency coefficient (from the mirror and the viewport).

The Photon Calibrator can be used to find the closed loop transfer function, as the Free-swinging Michelson method, or to calibrate directly the voice coil actuators. During S6, the main purpose of the Photon Calibrator was to assess the long-term stability of the calibration of the DCE channel. To determine the voice coil actuation function, the Photon Calibrator and the voice coil actuators sinusoidally dither the position of the optic while the interferometer

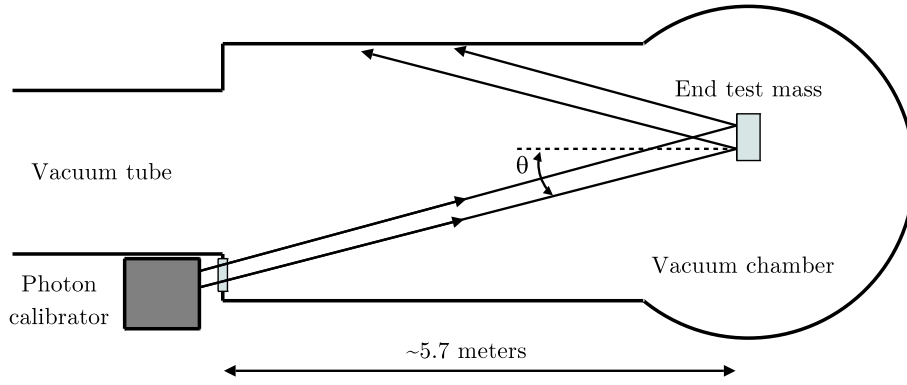


Figure 2.2: The Photon Calibrator global layout during S6. The optical table is located outside the vacuum envelope at the end station of the X arm. The two beams enter the vacuum via a viewport, then reach the end test mass, with an angle of incidence θ , and excite the mirror [5].

is operating in the Science Mode configuration. The sine wave frequencies of the two excitations are separated by 7.1 Hz, close enough to minimize differences in the response of the interferometer, but far enough apart to minimize two cross-contamination by the induced length modulations.

	DCE	Pcal
H1	393.1 Hz	400.2 Hz
L1	396.7 Hz	403.8 Hz

Table 2.1: Excitation frequencies for the Photon Calibrator and the DARM Control Excitation for both the interferometers.

Both actuation are detected by the instrument as a length modulation, and the signal appears as a peak above noise in the amplitude spectral density of the DARM error signal. During the measurement, the peaks in the excitation channels are also measured.

2.3 Computing the voice coil actuation coefficient

Using the solution of the equation of motion for the mirror, equation (2.7), we calculated the absolute displacement caused by the recoil of the photons. The amplitude of the signal from the internal photodetector of the Photon Calibrator (*Pcal laser peak*) measures the power of the auxiliary laser in counts.¹ To obtain the absolute power directed to the end test mass we calibrate separately the internal power monitor, via the measure of its calibration coefficient η , expressed in W/ct_{Pcal} . Thus, the amplitude of the power modulation, P_m (see

¹From now on we will use the abbreviation ct to indicate the counts of any digital signal, and $ct_{channel\ name}$ to indicate the source channel.

equation (2.1)), is given by

$$P_m = P_{cal \text{ laser peak}} \cdot \eta \quad (2.8)$$

This power readout can be used, via the equation (2.7), to determine the displacement of the mirror in meters. The ratio between this fiducial and the amplitude of the corresponding peak in the DARM error (*DARM Pcal peak*), which has the same frequency of the power modulation of the Photon Calibrator laser f_{Pcal} , leads to the calibration of the DARM error signal (*DE*) at the frequency of the modulation, expressed in m/ct_{DE} .

$$DE_{-cal}|_{Pcal} = \frac{2 P_m \cos \theta}{Mc (2\pi f_{Pcal})^2} \cdot \frac{1}{DARM \text{ Pcal peak}} \quad (2.9)$$

Using the response function $R(f)$ of the interferometer, expressed in m/ct_{DE} , and the DE calibration coefficient at the Photon Calibrator frequency, given by equation (2.9), we can calculate the calibration coefficient at any frequency. Because we want to compare the Photon Calibrator and the DCE excitations, we calculated the coefficient at the DCE excitation frequency (f_{DCE}).

$$DE_{-cal}|_{DCE} = DE_{-cal}|_{Pcal} \cdot \frac{R(f_{DCE})}{R(f_{Pcal})} \quad (2.10)$$

Our goal was to calibrate the DCE channel, not the DE. Therefore, we compared this calibration of the DARM error with the amplitude of the peaks at the DCE excitation frequencies in both the DE signal (*DARM DCE peak*) and the excitation monitor (*DCE coil excitation*). Taking the ratio of these peaks yields the transfer coefficient that converts the DE calibration to the DCE calibration, at the same frequency.

$$DCE_{-cal}|_{DCE} = DE_{-cal}|_{DCE} \cdot \frac{DARM \text{ DCE peak}}{DCE \text{ coil excitation}} \quad (2.11)$$

To provide a calibration coefficient that allows calibration of the DCE signal at any frequency by multiplying this coefficient by the DCE readout and the corresponding frequency squared, we multiply this coefficient, in the eq. (2.11), by the DCE excitation frequency squared:

$$DCE_{-cal}|_{1 \text{ Hz}} = DCE_{-cal}|_{DCE} \cdot (f_{DCE})^2 \quad (2.12)$$

Equation (2.12) gives the calibration coefficient of the DCE channel, expressed in m/ct_{DCE} . Because the DCE excitation is injected at the input of the voice coil actuation chain, it induces a length variation that can be compared to the length variation induced by the Photon Calibrator. Thus, comparison of the amplitudes of the two excitation peaks provides the direct calibration of the voice coils actuators of the interferometer. The calibration coefficient can

be also expressed in terms of the ratio of the amplitudes of the peaks as:

$$DCE_{-cal}|_{1 \text{ Hz}} = \frac{\frac{Pcal \text{ laser peak}}{DARM \text{ Pcal peak}}}{\frac{DCE \text{ coil excitation}}{DARM \text{ DCE peak}}} \cdot \frac{R(f_{DCE})}{R(f_{Pcal})} \cdot \frac{2 \eta \cos \theta}{Mc (2\pi f_{Pcal})^2} \cdot (f_{DCE})^2 \quad (2.13)$$

The Photon Calibrator can be used either to determine the DE sensitivity directly or to measure the voice coil actuation function, via the method outlined above. A key advantage of the Photon Calibrator is that it can be used while the interferometer is in Science Mode. Data were collected with this method during the entire S6 Science Run. Characterization of this Photon Calibrator data from LIGO's sixth Science Run is the subject of this thesis.

2.4 The Photon Calibrator Code

To analyze this stream of data from the Photon Calibrator, Dr. Roberto Grosso, from the Universität of Erlangen-Nürnberg, Germany, has written a C++ program, which calculates calibration quantities and some other statistic parameters that could be useful for a better analysis. We called this program Photon Calibrator Code or PCalCode. This software is continuously running on the Caltech computer clusters and provides a text file as output, which contains one row per minute and 31 columns. This script calculates the two excitation values for both the Photon Calibrator laser and the voice coil actuator, and also the two corresponding amplitudes into the DARM signal. The DARM error channel has a sampling frequency of 16384 Hz, thus for every minute this channel outputs $16384 \cdot 60 = 983040$ samples. The program takes all these values; calculates the Fast Fourier Transform of all the bins; filters them with a band-pass window, centered on the required excitation frequency; estimates the noise floor by calculating the mean of the points from adjacent frequencies; measures the peak value and then outputs the peak amplitude without the noise. All those calculations are repeated for every minute of data. For this characterization work, we looked only at the following columns:

1. GPStime – it is the number of seconds since 1/1/1970 12:00:00 AM UTC. This time measurement system is used in the GPS devices, thus the name.
2. StateVector – it is a binary number of 16 bits that summarizes the status of the interferometer. When the instrument is in Science Mode, the state vector is $(FFFF)_{16}$ or 65535.
3. DCExc – it is the amplitude value of the length modulation injected into the coil actuators (*DCE coil excitation* in the eq. (2.13)).

5. `DE_DCE_raw` – it is the peak amplitude in the DARM error at the frequency of the coil excitation (*DARM DCE peak* in the eq. (2.13)).
7. `Pcal` – it is the power of the Photon Calibrator laser, measured by the internal photodetector (*Pcal laser peak* in the eq. (2.13)).
9. `DE_Pcal_raw` – it is the peak amplitude in the DARM error at the frequency of the Photon Calibrator laser modulation. (*DARM Pcal peak* in the eq. (2.13)).
25. `DE_Pcal_rawNoiseEstimate` – it is the noise in the DARM error at the Photon Calibrator modulation frequency. The noise floor is estimated via a linear fit of the the 5 nearest points outside the excitation frequency, on both sides.

There are two text files, one for the data from the Hanford interferometer and one for the data from the Livingston interferometer. At the time of this writing, both the text file are updated to July 27, 2010 and contain every minute of data since the begin of the S6 Run. Of course only the times in which the interferometer was in Science Mode are taken for this analysis.

	Total	Science
H1	545594	265468
L1	543585	231656

Table 2.2: Total minutes of data and Science Mode data for both the interferometers.

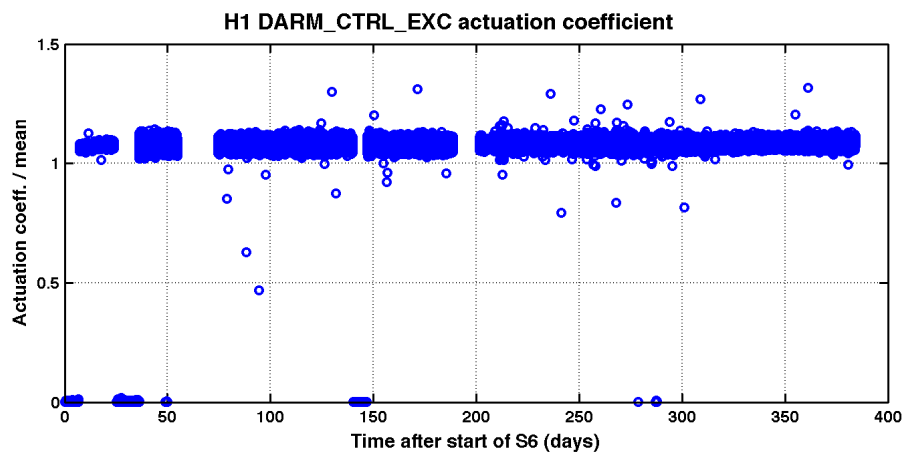
To plot those data and to analyze them, we used and modified a MATLAB script, originally written by Dr. Richard Savage, Dr. Greg Mendell and Jonathan Berliner. This program removes all the entries in which the interferometer was not in Science Mode, and computes the calibration coefficient basing on the equation (2.13).

Chapter 3

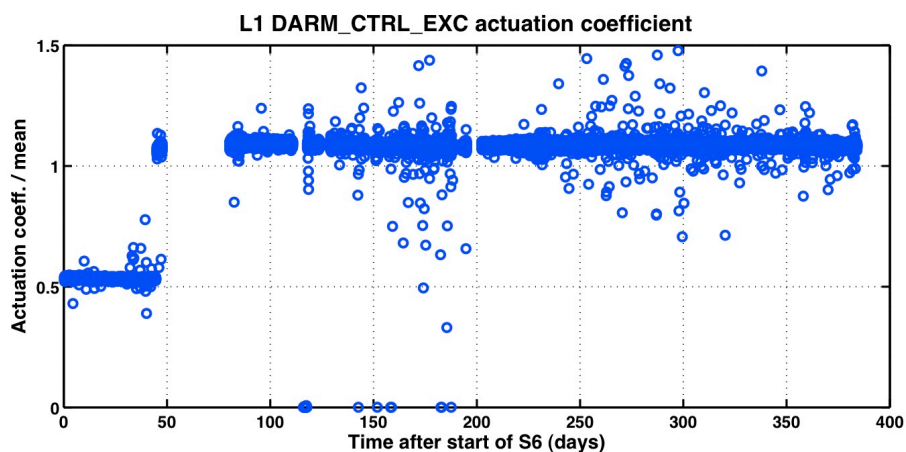
Characterization of the data

3.1 Removing outliers

In the figure (3.1) the result of the calculations done by the PcalCode for all of the S6 data are plotted. First, we removed the data from the days in



(a) Hanford



(b) Livingston

Figure 3.1: The calibration coefficient computed for all the minutes of Science Mode during S6. The biggest outliers are not shown.

which there were known problems in the interferometers, such as non-standard detector setups, maintenance work and other known issues. For example, the first 80 days of the Run for L1 cannot be used for this characterization due to a faulty connection inside the photodetector. Then, we removed all the time

	Before	After	Removed	Removed %
H1	265468	251404	14064	5.3%
L1	231656	194893	36763	15.9%

Table 3.1: Points removed because of known issues of the interferometer.

intervals during which the Photon Calibrator laser was turned off (or for some other reason unreadable). The results are shown in figure (3.2). After that, some large glitches were still evident in the calibration plots.¹

	Before	After	Removed	Removed %
H1	251404	233725	17679	7.0%
L1	194893	193910	983	0.5%

Table 3.2: Points removed because of Photon Calibrator laser unable to reach the internal power monitor.

To veto the glitches, we looked at the other columns of the text file for the same GPS time, comparing all the values with the previous and the next row. A field that seems to be affected by the glitches is one of the noise levels calculated by PCalCode: the `DE_Pcal_rawNoiseEstimate`. After more manual inspections, we removed all the points that had a noise value greater than a certain threshold, scaling the threshold with the noise level within the same day. The characterization of this veto is in the table 3.4.

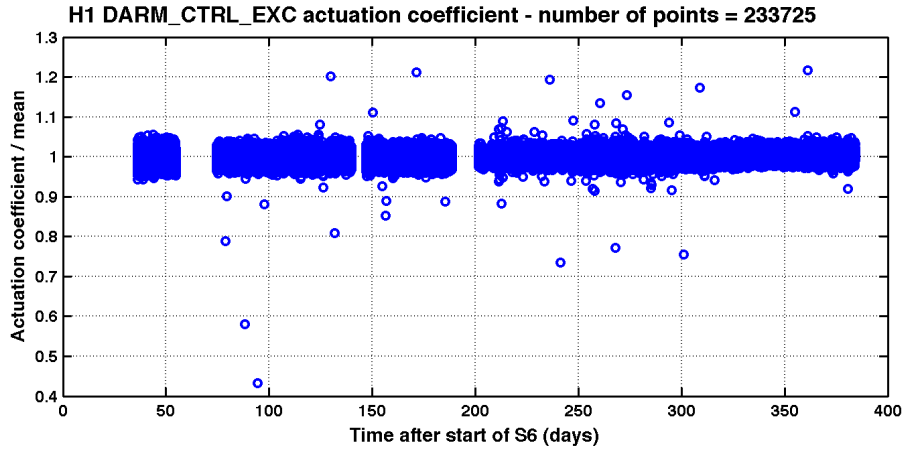
	Thresholds	Before	After	Removed	Removed %
H1	$\mu \pm 5\sigma$	233725	233194	531	0.2%
L1	$\mu \pm 5\sigma$	193910	192902	1008	0.5%

Table 3.3: Points removed by `DE_Pcal_rawNoiseEstimate` veto.

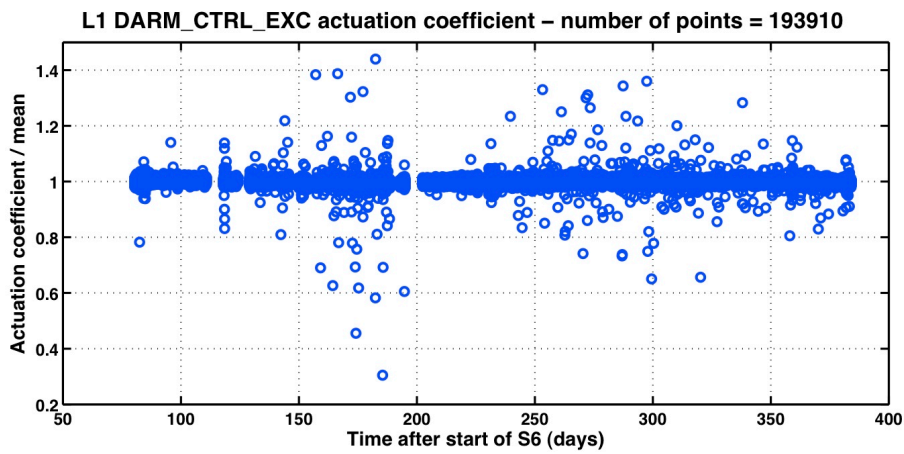
Due to the low accuracy of the veto, we decided not to apply it. Instead, we applied a statistical criterion to remove the outliers. We calculated the number of points outside n standard deviations (σ) from the mean, and compared the results with what would be expected if the data were normally distributed. See table (3.5) for further details.

Outside three standard deviations from the mean, there were a factor of 2 or 3 times more outliers in the data than would be expected for a Normal

¹A glitch is a transient in a data channel, which usually lasts less than a second. In many cases a glitch is recorded by more than one sensors at the same time. This often allows a better identification of what caused it.



(a) Hanford



(b) Livingston

Figure 3.2: The calibration coefficients, after the known issues times removal.

	Removed	Outl.rem.	Outl. tot.	Accuracy %	Efficiency %
H1	531	41	58	7.7%	70.7%
L1	1008	278	378	27.6%	73.5%

Table 3.4: Characterization of the DE_Pcal_rawNoiseEstimate veto. The accuracy is the ratio between the number of removed outliers and the number of points removed. The efficiency is the ratio between the number of outliers removed and the total number of outliers in the data.

Distribution. Because the additional outliers only represented less than 1% of the data, we removed a-priori all the points that were three standard deviations below and above the mean of their day, and focused on the rest of the points for this characterization work.²

In figure (3.3) the normalized plots of the calibration coefficients for both interferometers after the filters are shown. The mean of the points within a

²We first removed the largest outliers (farther than 10σ) before to calculate the means and the standard deviations.

σ	Pcal data		Normal distribution	
	H1	L1	H1	L1
2	10861	8900	10672	8854
	4.66%	4.63%	4.56%	
3	821	1515	631	524
	0.35%	0.78%	0.26%	
4	104	405	15	12
	0.05%	0.21%	0.006%	
5	57	298	0	0
	0.02%	0.15%	$5 \cdot 10^{-7}\%$	

Table 3.5: Comparison of the number of the outliers for the data and a sample with the same number of points generated using a Normal Distribution.

	Before	After	Removed	Removed %
H1	233725	232904	821	0.35%
L1	193910	192395	1515	0.78%

Table 3.6: Points outside 3σ from the daily mean

	Mean	σ
H1	$1.28 \cdot 10^{-9}$ m/ct	$1.39 \cdot 10^{-11}$ m/ct
L1	$1.08 \cdot 10^{-9}$ m/ct	$0.64 \cdot 10^{-11}$ m/ct

Table 3.7: Statistical quantities of the data

day is plotted as a red line, while the green lines are three standard deviation above and below the mean of the day. The yellow dashed line represent the mean of the whole Science Run.

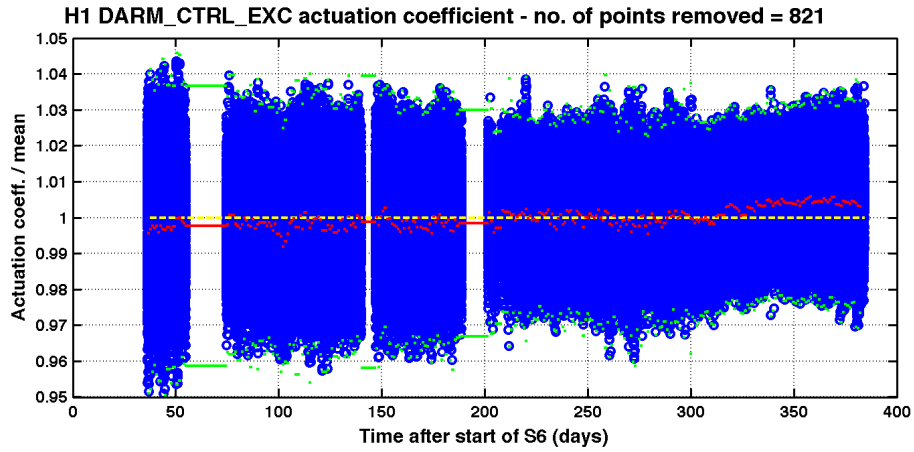
3.2 Identification of a linear trend in the data

Looking at the data from H1, a small increasing trend is visible, especially in the last part. We fit those data with a linear regression.

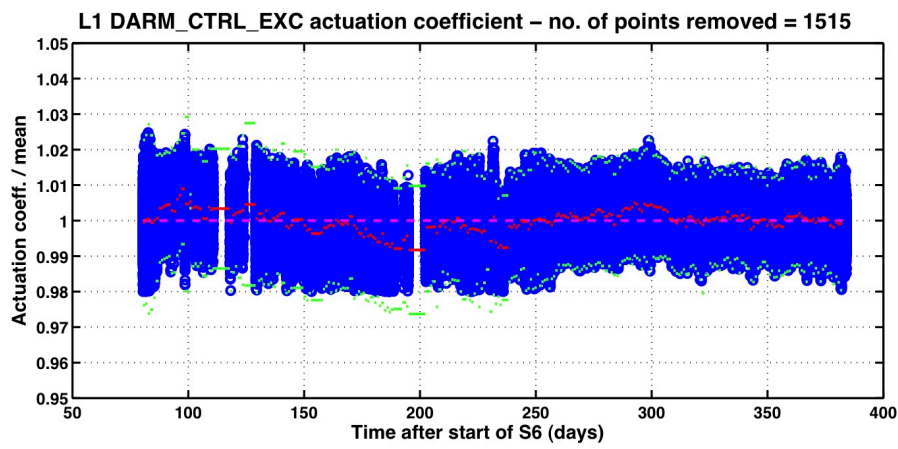
The results of the fit are shown in the figure (3.4). One of the advantages of the identification of a trend in the data, is that the data quality can be improved by removing the trend from those. We removed the linear trend to calculate the statistical distribution of the data in the paragraph 3.3.

Looking at the figure (3.5) from L1, there is no evident increasing or decreasing linear trend in the data. The long-term variations are larger, but the overall linear trend is smaller than in the H1 data.

The parameters of the fit are shown in the table 3.8. The high dispersion of the data is causing the low χ^2 values for both the regressions.



(a) Hanford



(b) Livingston

Figure 3.3: The calibration coefficients for the S6, after the removal of the outliers.

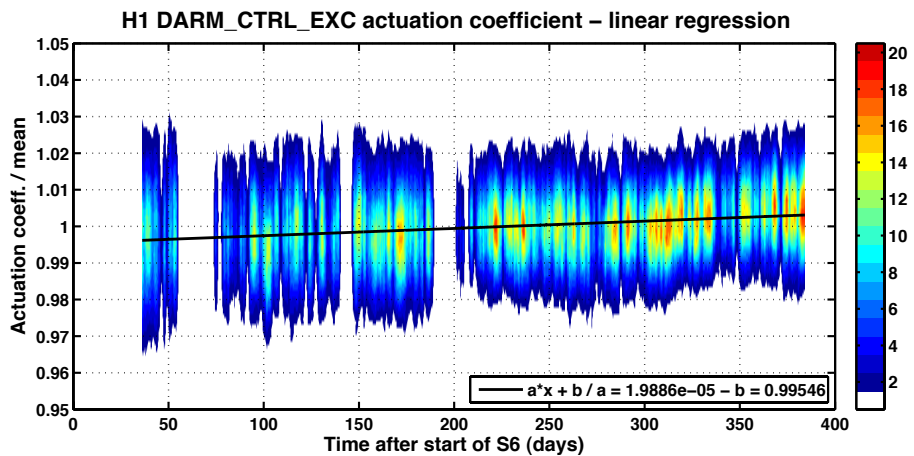


Figure 3.4: Linear fit of the data from Hanford. The density of points is represented using a color scale.

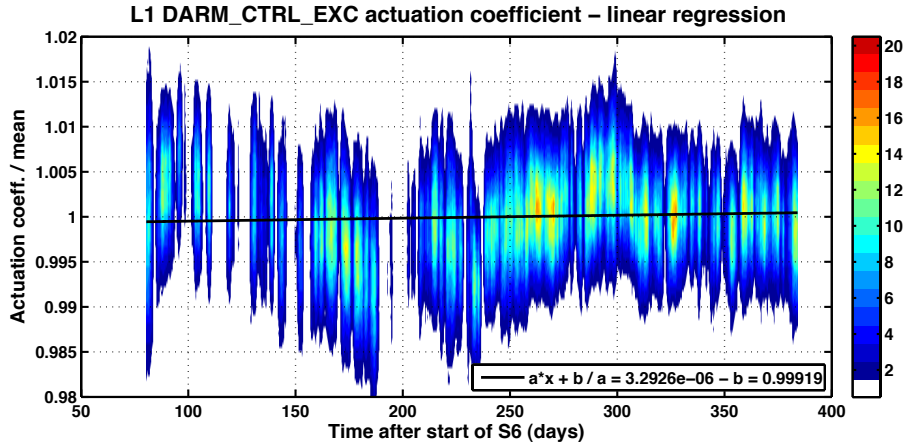


Figure 3.5: Linear fit of the data from Livingston. The density of points is represented using a color scale.

	a	b	ν	χ^2
H1	$1.99 \cdot 10^{-5}$	0.995	232902	26.17
L1	$0.33 \cdot 10^{-5}$	0.999	192393	6.76

Table 3.8: Linear regression results – model: $(ax + b) - x$ are S6 days

3.3 Statistical description of the data

We reported the histograms (3.6) of the calibration data, without the outliers, for both H1 and L1 data. All the values are divided in 100 intervals and the occurrences of every interval are counted and reported in the plots. The histogram for H1 is made with the data obtained after the removal of the linear trend.

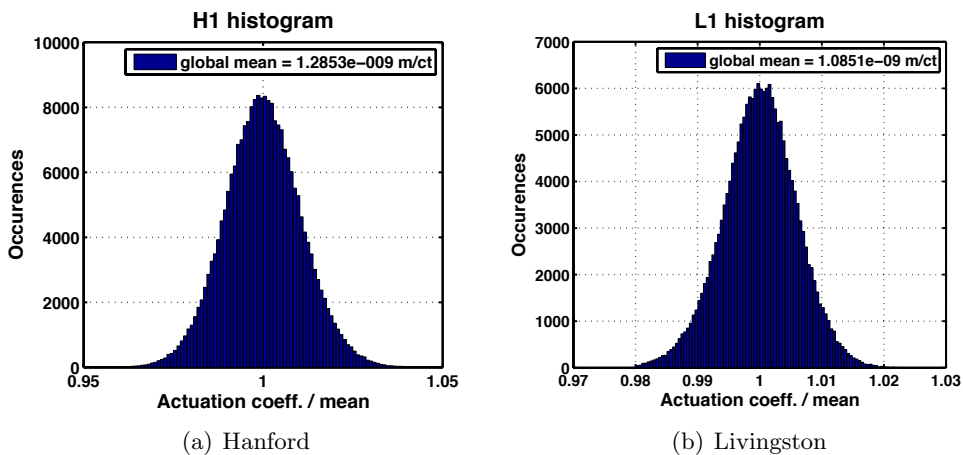


Figure 3.6: Histograms of the calibration coefficients.

We fit those histograms with a Normal Distribution, using the least-squares method. First, the occurrences were normalized by the constraint that the area

below the points was about 1. To calculate a rough estimate of the area we chose to use the trapezoidal rule. Then the values of the calibration coefficient were normalized dividing by their mean, so we expect from the fits a mean value of about 1. Thus, we can take the Normal Distribution as model

$$f(x) = \frac{1}{\sqrt{2\pi\sigma^2}} \cdot e^{-\frac{(x-\mu)^2}{2\sigma^2}} \quad (3.1)$$

In figure (3.7) there are the histograms of the calibration coefficient after the normalization described above. Both the histograms were fitted with the equation (3.1) as model.

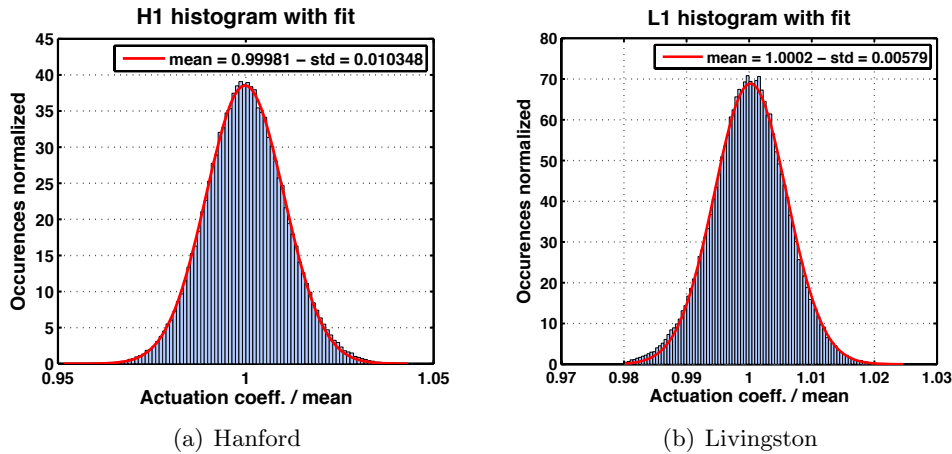


Figure 3.7: Normalized histograms of the calibration coefficients, with the fit using a Normal Distribution as model.

The output parameters of the fits are in the table (3.9).

	Norm.	μ	$\Delta\mu$	σ	$\Delta\sigma$	ν	χ^2
H1	$4.67 \cdot 10^{-3}$	0.99981	$3 \cdot 10^{-5}$	0.01035	$2 \cdot 10^{-5}$	98	119.35
L1	$1.16 \cdot 10^{-2}$	1.0002	$3 \cdot 10^{-5}$	0.00579	$2 \cdot 10^{-5}$	98	9.47

Table 3.9: Parameters and goodness of the fits

Using the result provided by the fits, it can be inferred from the χ^2 test that the H1 data (apart from the noise) are normally distributed with a probability of 90% and the L1 data are normally distributed with a probability of 5%.

3.4 Averaging the data

To provide a better visualization of the data, we grouped the data into single points and plot the mean value of the groups of points. This is more useful than the raw data points for identifying long-term trends. Thus, for each mean value we want to plot error bars that represent the plus and minus one standard deviation estimate of the error of the mean. The usual estimator of the error

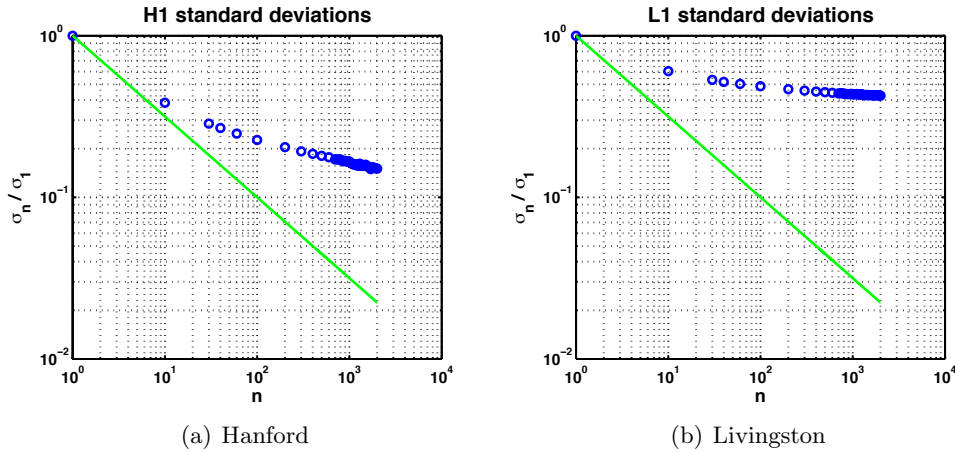


Figure 3.8: Error improvement diagrams for the calibration coefficients. The scale is logarithmic for both the axes. The blue points are the standard deviations of the means of the samples in which we divided the data, for different sample widths. The green line is $1/\sqrt{n}$, which is how the Standard Error of the Mean improves.

of the mean is called Standard Error of the Mean, and is calculated as

$$\sigma_n = \frac{\sigma_1}{\sqrt{n}} \quad (3.2)$$

where σ_1 is the standard deviation of the raw data, n is the number of data points within a sample and σ_n is the standard deviation of the means of the groups of samples. We calculated σ_n for various values of n , to see if the error really improves as the square root of the number of points within each sample.

For each value of n , we divided the data in samples of n points. Then, we calculated the mean of each sample and the standard deviation of the means.

Each point of figure (3.8) is obtained dividing the standard deviations of the sample means by the standard deviation of the raw data. The green lines in figure (3.8) are $1/\sqrt{n}$, which is what we expect for the Standard Error of the Mean. Clearly, the points do not follow those lines; the uncertainty in the estimates of the means improves more slowly than the square root of the number of points, even though the histograms were closely modeled by Normal Distributions.

The Standard Error of the Mean can be used only if the data within different samples are uncorrelated, otherwise one must consider the cross-correlation contributions to the improvement of the error. During the construction of a histogram, all the points are grouped in different bins looking only at their value, no matter when that point occurred in time. So, a temporal correlation in the data cannot be seen in a histogram and thus cannot influence the results of the fits.

To find out if there is a temporal correlation in our data, we randomized

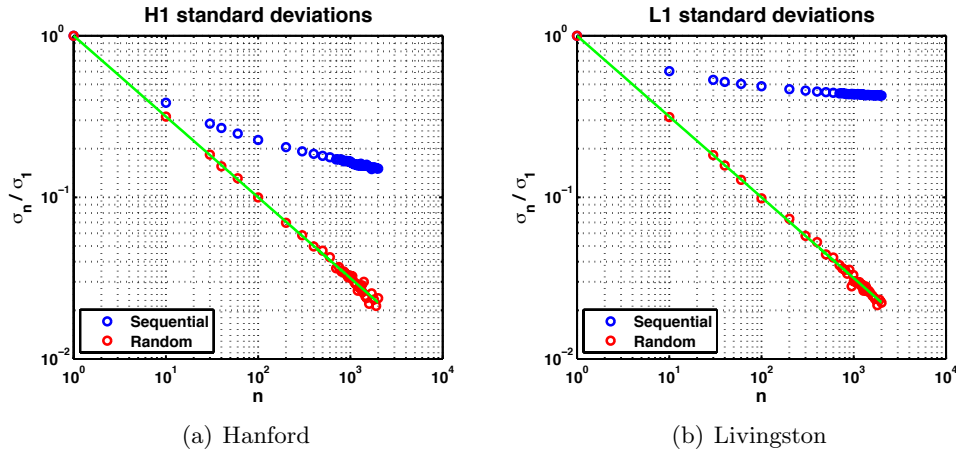


Figure 3.9: Comparisons of the improvement of the error between the calibration data and the random selected data. The red points are the standard deviation of the means of the samples, selected in a random way in time.

the order of the samples. Instead of choosing points sequentially, we chose the points randomly to build each sample. Thus, all the values of the points are the same, just chosen in a random order. We then repeated the previous calculation with the randomized data. The results are shown by the red circles in figure (3.9).

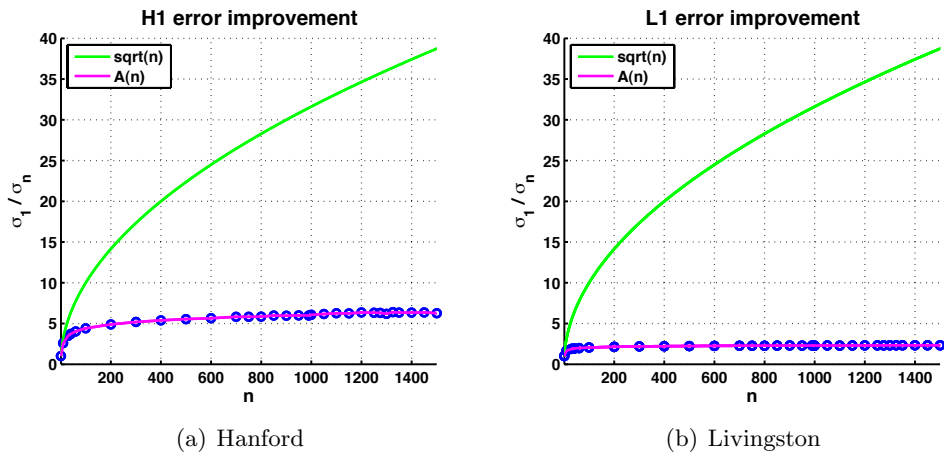


Figure 3.10: Error bar sizes interpolating functions. The purple line is the interpolating function $A(n)$ used to calculate the error bars for every sample width.

Because the data are correlated, we cannot use the Standard Error of the Meant to estimate the error bars for the averages. Using the calculated values of σ_n for the sequential data, we can interpolate to give a function, $A(n)$, that can be used to estimate error bars for any value of n .

$$\sigma_n = \frac{\sigma_1}{A(n)} \tag{3.3}$$

The results of the interpolation are shown in figure (3.10). For both the interferometers our interpolating function was smaller than the square root of the number, which means that the error of our averages improved less than the Standard Error of the Mean, due to the correlation. Thus, the error bars in the following plots are several time larger than the error bars calculated using the Standard Error of the Mean.

3.5 Long-term trend plots with averaged data

To better visualize the long-term trends in the data we first divided the data into hour-long segments and then into day-long segments.

In figure (3.11), all the data are divided in segments of one hour long. Only contiguous Science Mode hours are taken, thus all the Science intervals shorter than 60 minutes are ignored in this plot. Every point is the mean value of

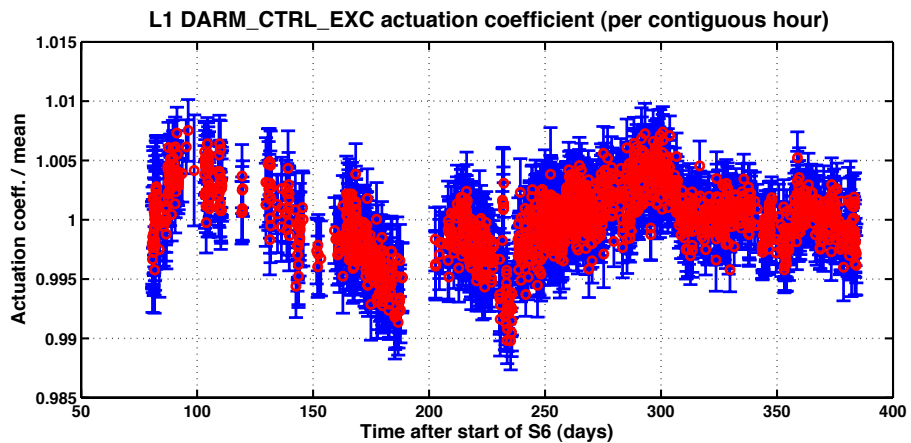
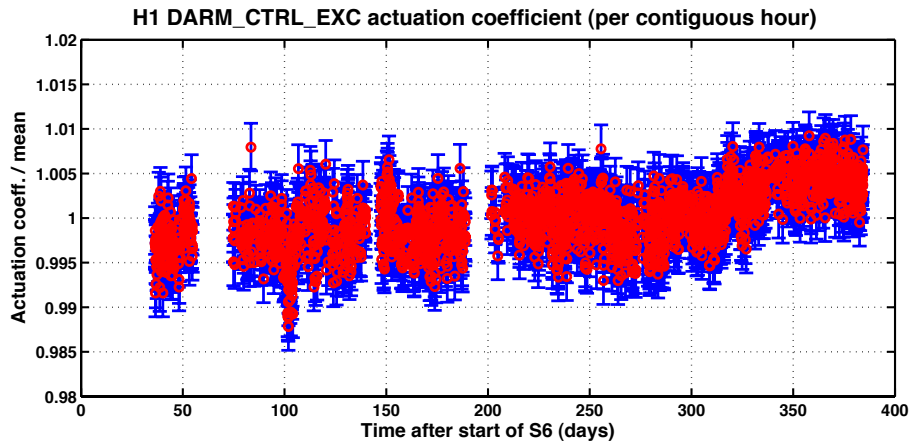
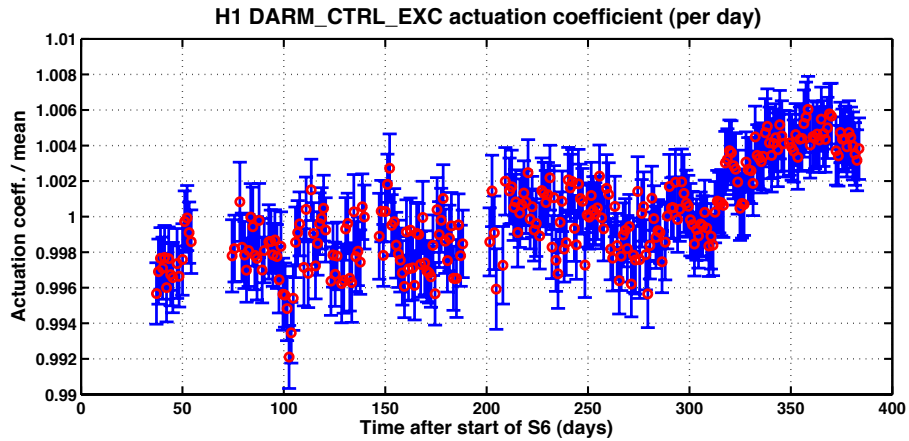


Figure 3.11: Calibration coefficients, grouped into hours. Each point represents a contiguous hour of Science data.

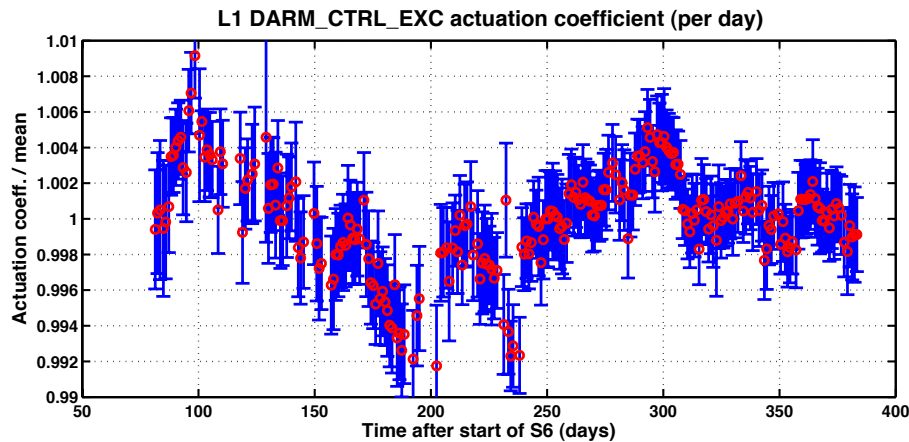
the 60 points within the hour, versus the mean time of the hour, expressed

in days from the beginning of S6, and has an error bar, estimated using the interpolating function calculated in the paragraph 3.4.

The figure (3.12) is obtained dividing the data into days instead of hours. This time, we removed the constraint of the adjacency of the data within an hour. The script takes all the points within a day and calculates their mean to generate a day point. Again, the error bars are calculated via the interpolating function obtained above.



(a) Hanford

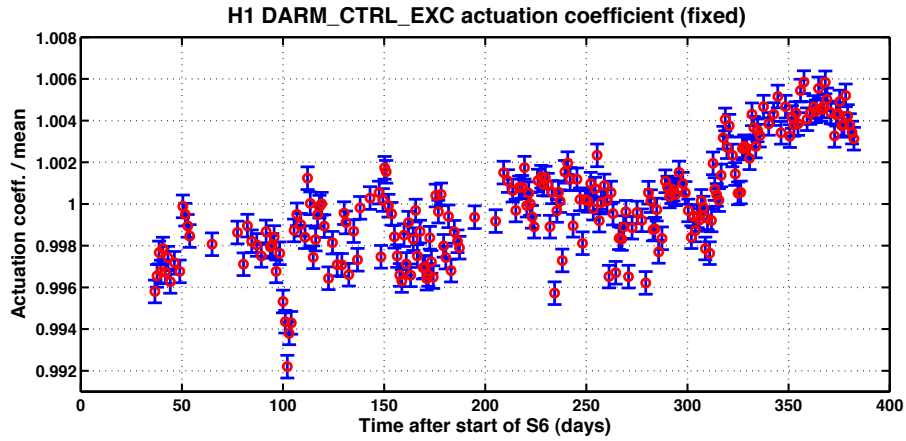


(b) Livingston

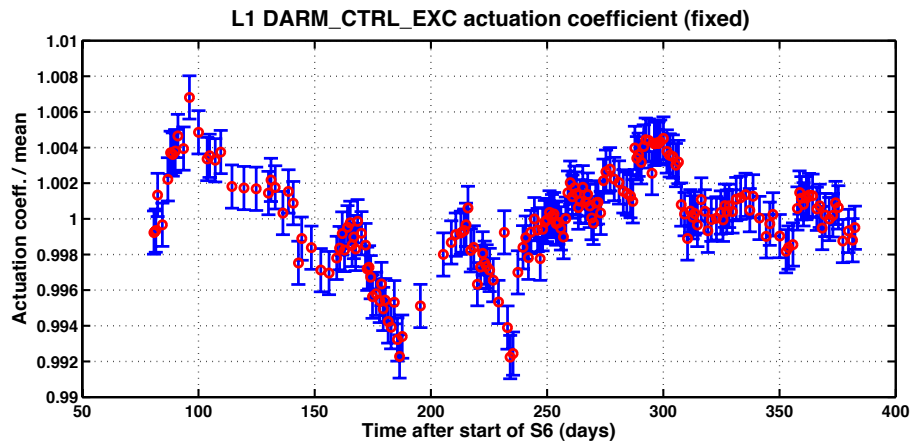
Figure 3.12: Calibration coefficients, grouped into days. Each point represents a day of Science data.

There is no obvious reason to divide the data in hours or in days, they are simply the convenient ways in which long spans of time can be divided. However, the arbitrary divisions introduce some other constraints, e.g. the contiguity of the data within an hour or the different amount of Science Mode within a day, which are not necessarily caused by the statistics of the data. Thus, we chose to provide a third plot (3.13), in which every point is made by the mean of 1000 measurements, without other constraints.

Every block of 1000 points is further improved by removing the worst 10



(a) Hanford



(b) Livingston

Figure 3.13: Calibration coefficients, grouped into blocks of 1000 points each one.

points in the block. To determine the worst points we used the Maximum Absolute Deviation from the mean of the vector of points x

$$MAD(x, i) = |x_i - \mu(x)| \quad (3.4)$$

where $\mu(x)$ is the mean of the block and x_i is an element of the vector.

The point which has the largest value of the quantity is removed from the block. This operation is repeated 10 times for every block. Thus, after this cleaning step, every block contains 990 measurements. Again, the abscissa is the mean time of the points within the block, expressed in days since the beginning of S6. The error bars are the same for every point, calculated using the interpolating function obtained in the paragraph 3.4.

Conclusions

In figures (3.12) and (3.13) long-term trends are visible, even though these trends are less than 1% and the two- σ variations of the 60-second-long FFT data are on the order of 5%. This enhanced visibility was achieved by grouping the data and plotting the mean values of the data groups. The plotted error bars were determined by a statistical characterization of the data and found to be several times larger than what would be predicted by the Standard Error of the Mean. The cause of the increased error bars was determined to be temporal correlations in the data.

Because the excitation frequencies of the Photon Calibrator and DARM Control excitations differ by 7.1 Hz, changes in the response function over this frequency span could lead to variations in the calibration coefficient. In this analysis, we did not include changes in the sensing function caused by the variations of the γ factor in the DARM loop sensing function (see figure (1.2)).

Another possible cause of variations in the DCE calibration coefficient is changes in the absolute power calibration of the internal photodetector of the Photon Calibrator. This photodetector is calibrated against a stable standard to provide an accurate measurement of the power modulation and thus of the displacement amplitude of the end test mass. Potential variations in the calibration coefficient η (see equation (2.8)) of this internal power monitor were not considered in this analysis [6].

The voice coil actuation coefficient, measured using the Photon Calibrator, is affected by the whole voice coil actuation chain, which includes, for both ETMs, the drivers, the coils near the optics, the digital filters and all the electrical connections. Variations in any of these could cause trends in the calibration data. Also, because the Photon Calibrator table is located outside the vacuum envelope (see figure (2.1)), the auxiliary laser beams pass through a viewport before they reach the mirror. The transmission of this viewport could change over the duration of the S6 Run (more than an year), due to contamination or to variations of its index of refraction caused by temperature changes inside the end station.

The overall goal of the Photon Calibrator during S6 was to quantify the long-term stability of the voice coil actuators. We analyzed more than one year of data from both LIGO observatories and found that the voice coil actuation

coefficients were stable to better than 1.4% peak to peak at H1 and 1.8% peak to peak at L1.

The stability of the actuation coefficients implies that the DARM actuation chain, for both the end test masses; the Photon Calibrator layout, including the internal power monitor, beam splitters, and the power modulator; the procedure applied – simultaneous excitation of the optic at two different frequencies via the Photon Calibrator and the DCE; and the sensing function of the interferometer, at both observatories, was stable at this level during all of the S6.

The analysis completed for this report satisfies the main goal of the S6 Photon Calibrator effort by quantifying the long-term trends in the voice coil actuation coefficients. Furthermore, the observed overall stability of the measurement procedure indicates that the Photon Calibrators are an attractive option for stable and accurate calibration of the next generation of gravitational wave detectors.

Bibliography

- [1] P. R. Saulson. *Fundamentals Of Interferometric Gravitational Wave Detectors*. World Scientific, Singapore, 1994.
- [2] The LIGO Scientific Collaboration. LIGO: The Laser Interferometer Gravitational-Wave Observatory. *Reports on Progress in Physics*, 72, 2009.
- [3] L. Lindblom. Optimal calibration accuracy for gravitational-wave detectors. *Physical Review D*, 80, 2009.
- [4] E. Goetz et al. Accurate calibration of test mass displacement in the LIGO interferometers. *Classical and Quantum Gravity*, 27, 2010.
- [5] E. Goetz et al. Precise calibration of LIGO test mass actuators using photon radiation pressure. *Classical and Quantum Gravity*, 26, 2009.
- [6] S. Erickson. Investigation of Variations in the Absolute Calibration of the Laser Power Sensors for the LIGO Photon Calibrators. Technical Report LIGO-T080316-00-W, LIGO, 2008.

Ringraziamenti

Quando si giunge alla fine di un percorso, si sente sempre la necessità di ringraziare le persone che ci hanno accompagnato lungo la strada, chi dall'inizio o chi soltanto alla fine.

Al Prof. Francesco Fidecaro vanno i miei più sentiti ringraziamenti, per aver reso possibile questo lavoro e per essersi sempre mostrato disponibile quando avevo bisogno del suo aiuto.

Also, I would like to say thank you to Dr. Rick Savage, for all the help he gave to me and to this work during the last three months. Without him, I would never be able to live this beautiful experience. And I think he tried to make me a better person, besides than a better physicist. I really hope to work with you again.

Un pensiero va al Prof. Riccardo DeSalvo, per avermi aiutato durante tutta questa esperienza. Grazie a lui mi sono sentito a casa anche a Pasadena, CA.

Desidero anche ringraziare tutta la mia famiglia, i miei genitori Carmelo e Gabriella e mia sorella Elena, per avermi permesso di studiare qui e per non aver mai smesso di sopportarmi e di volermi bene.

Un ringraziamento particolare va a Stefania, per aver condiviso con me tutto questo cammino universitario e per avermi aiutato a non arrendermi mai davanti alle difficoltà che lo hanno spesso segnato.

Infine, sento di dover ringraziare anche tutti gli amici che ho conosciuto in questi anni, e che ogni tanto mi hanno fatto dimenticare gli oneri della vita universitaria. Un grazie speciale va a tutti voi che avete reso e che ogni giorno rendete felice la mia permanenza a Pisa.